Paper 15

Advances in Electromagnetic Data Processing: Noise, Signal, SPM and AIP

Macnae, J. [1]

1. RMIT University, School of Science, GPO Box 2476, Melbourne 3001 Victoria, Australia

ABSTRACT

Most of the breakthroughs in electromagnetic (EM) geophysical data processing in the past decade have been in the data-rich field of airborne electromagnetic (AEM) surveys. These advances have progressed on five separate fronts: signal, noise, superparamagnetism (SPM), inductive induced polarization (IP), calibration and quality control (QC). Signal characterization studies have allowed quantitative corrections to signal distortions in the early delay time, producing dynamically corrected data more consistent with modelling. Composite waveforms have been used to fill spectral gaps in simpler transmissions. More recently, full waveform modelling and inversion has improved on earlier approximations to actual waveforms, producing excellent fits to "raw" data exactly as measured. Noise has been reduced on several fronts: there have been improvements to electronics and sensor intrinsic noise, rotation noise has been reduced through novel suspension systems, and strategies devised and advanced for the removal of unwanted signals, predictable or transient in nature. Partially or exactly predictable but unwanted signals may arise from the powerline network, from cultural conductors such as pipelines or fences or components of the AEM system itself; and from submarine very low frequency (VLF) communications. Transient signals most commonly come from sferic activity, the sources of which are now extensively monitored. AEM primarily has been used in the past to estimate conductivity, to a lesser extent static magnetic permeability and minimally for dielectric permittivity. Recent processing developments that allow for frequency dependent physical properties can now provide estimates of superparamagnetic susceptibilities and Cole-Cole IP parameters. The IP parameters include DC or preferably AC conductivity, with three additional parameters including chargeability reasonably well defined but with very limited resolution of the frequency dependence and Cole-Cole time-constant.

Future advances in processing are still needed to permit operation of AEM and airborne IP (AIP) systems at much lower base frequencies than the current 25 Hz limit for good AEM data. Very limited advance is expected in terms of airborne transmitter output, specifically dipole moment and current stability in the immediate future. Significant advances however should come through rotation or rotation rate monitoring of sensors, where preliminary results have been very positive. Alternatively, several research groups have been attempting the mechanical isolation of sensors from rotation excitations, using fluid suspension systems. Total field magnetic sensors with limited bandwidth have been used to eliminate airborne rotation noise, but are limited to measuring one magnetic component in the direction of the earth's field. A worthwhile advance proven in theory in the 1990s but only implemented in data acquisition for the ZTEM airborne tilt-angle system is the use of local and remote EM base-stations to help predict and hence remove the effects of unwanted signals.

INTRODUCTION

Airborne electromagnetics (AEM) is a very important tool in mineral exploration, as it provides physical property information at much higher resolution than gravity or gravity gradiometry and more accurate depth information than either of magnetics or the gravity variants. The history of AEM is littered with different systems (Fountain, 1998), each with distinct characteristics, with variable dipole moment, transmitter waveform, system geometry, sensor, navigation, data acquisition and sampling. By far the majority of systems in operation at present for detailed mineral exploration and hydro-geophysical surveys are time-domain, closely-spaced transmitter-sensor (called double-dipole; Macnae, 2016b) systems towed beneath helicopters. Regional surveys often use time-domain fixed-wing aircraft with the sensor in a towed- bird, systems that are cost-effective for large surveys. A few frequency domain systems, either helicopter towed bird or wing-tip geometry, still operate.

Once data have been acquired and processed to a few time channels or frequency responses, geological interpretation requires a step where the responses in amplitude vs time or frequency are converted to conductivity-depth. This conversion may be through fast approximate methods, which I classify as processing, or through formal inversion methods requiring initial models and model constraints. I will not discuss inversion in this review.

This review will concentrate on the changes in time-domain AEM data processing over the past decade, and is not intended to be an objective summary of the history or "state of the art". These processing changes have been driven by major improvements in hardware and sensor suspensions that have increased signal to noise ratios by an order of magnitude or more in many AEM systems over the last 15 years. I will focus on five processing topics in this review. 1) Improvements in data acquisition and processing through noise suppression; and 2) signal enhancement in different AEM systems form the first two topics. Next, 3) the effects of superparamagnetism (SPM) and 4) induced polarization (IP) on airborne data will be discussed, particularly newly developed processing developments to separate and separately interpret the EM, SPM and airborne IP (AIP) contributions to the observed response. Finally, 5) calibration and quality control (QC) will be discussed.

In "Proceedings of Exploration 17: Sixth Decennial International Conference on Mineral Exploration" edited by V. Tschirhart and M.D. Thomas, 2017, p. 191–208

The completeness of a review in this field is limited by contractor secrecy: most airborne contractors have proprietary processing and "trade-secret" noise reduction methods. Confidentiality agreements cover some of the systems I have worked on, limiting my ability to detail some developments. In the case of one now long-dissolved company, proprietary noise reduction software consisted of successively running a 3-point averaging filter through the data until noise specifications in ppm were met. No wonder this method was secret! Even today, the amount of data averaging and the nature of the tapering windows are often reluctantly or never disclosed. This information however is critical for accurate 2D and 3D inversions.

I have worked on the processing algorithms of Spectrem, Tempest, VTEM, and BIPTEM (Macnae et al, 2017) AEM systems. I am also familiar with the data of many others through customization of system descriptors for conductivity-depth-imaging (CDI). With so many publication avenues these days, confidential survey reports, search engines and abstracting services have provided relevant information for systems with which I am not as personally familiar.

The noise-minimized and corrected or compensated decays produced from processing are used to predict physical properties within the earth. Historically, the means for extracting these physical properties has evolved from picking "anomalies" or bumps in profile plots last century, to routine generation of stitched 1D sections of conductivity this century, with wire-loop inversions at anomalies (Macnae, 2007). In the last decade, progress to fitting anomalies with approximate 2D or 3D models has been made (Fullagar et al., 2015, Kolaj and Smith, 2017), and most recently has involved identifying and correcting for the effects of SPM and IP.

This paper will first discuss noise in airborne data. A discussion of signal, specifically the choice of waveform will follow. AEM primarily has been used in the past to estimate conductivity, to a lesser extent static magnetic permeability, and minimally for dielectric permittivity (Huang and Fraser, 2001). Recent processing developments allow for frequency dependent physical properties can now provide estimates of superparamagnetic susceptibilities and Cole-Cole IP parameters, as described in the two subsequent sections. Finally, the paper will look at the important processing issues of calibration and data quality control, illustrating some of the issues with a comparison of survey data between 2 systems.

1: NOISE SUPPRESSION

Raw Data Examples

A few examples of signal, unwanted signal, and noise are illustrated in Figure 1, showing one full-wave sample of airborne B field data collected at 12.5 Hz at some distance from a powerline. A non-zero, non-linear background has been fitted and subtracted from this data to allow useful plotting on a linlog amplitude scale. High frequency noise is evident in the transmitter off-time, consisting of: 1) occasional (large) sferics, and 2) a combination of unwanted very low frequency (VLF) signals and sensor / data acquisition system noise. Because of the linlog plotting scale on the y-axis, this noise is only evident near the zero-amplitude axis on the plot. The transmitter in this case has 3) an exponential turn-on and a rapid turn off at both time zero and at 4) the midpoint of a complete cycle. However, as loop resistance changes with temperature, and with stray capacitance effects, the turn-off is far from exactly repeatable and due to bandwidth limitations (Schamper et al., 2014) can be seen 5) in detail not to be instantaneous at transmitter time zero.

Plotting time zero in Figure 1 (at 0 and 80 ms) is set at the time of an electronic trigger that caused the transmitter current to start is turned off. The current turn-off is finite in duration and the measured response further delayed by receiver bandwidth, as any finite bandwidth introduces a delay between Tx waveform and that sensed by the Rx (Schamper et al., 2014). The mid-point of the observed turn-off response, at high altitude, on a linear scale, is a better physical indicator of effective time zero rather than the electronic definition of the transmitter current trigger for an AEM system. Processing aims to correct for small changes in the very early time around geophysical time zero, including the effect of jitter between the transmitter and receiver clocks. Good transmitters have very repeatable waveforms, but bucked transmitters tend to create inconsistent residual primary fields as detected at the receiver (Figure 2). A process called compensation can correct such variations. Choice of waveform repetition rate is such that simple stacking can eliminate powerline harmonics, which otherwise can dominate received signals.

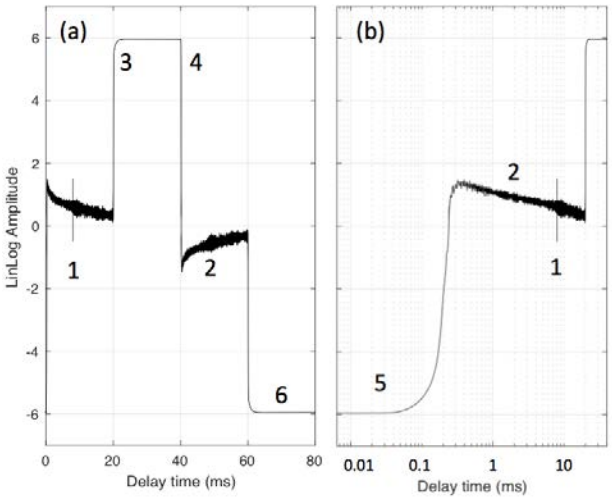

Figure 1: B field 156.25 kHz streamed AEM data with linlog amplitude plotted for a full cycle on linear (a) and for a half-cycle on logarithmic (b) time scales to highlight some processing issues. The base frequency is 12.5 Hz, and plot time 0 is defined as the start of the transmitter turn-off. See text for a description of the numbered features.

In many time-domain airborne systems, a bucking loop carrying a reversed current to the main loops is used, such that the field observed at its centre is close to zero. Due to "antenna effects" from parasitic capacitance, some of the high-frequency components of the transmitted current escape as displacement currents and as a result, the current in the bucking coil is slightly different from that in the main current loop. Changes to bucking

fraction are caused by very small relative motions of transmitter, bucking coil and receiver leads to variable amounts of primary field being detected by the receiver. Modelling almost invariably assumes the primary field is of the form of waveform in Figure 2a, and ignores the small distortions seen in 2b.

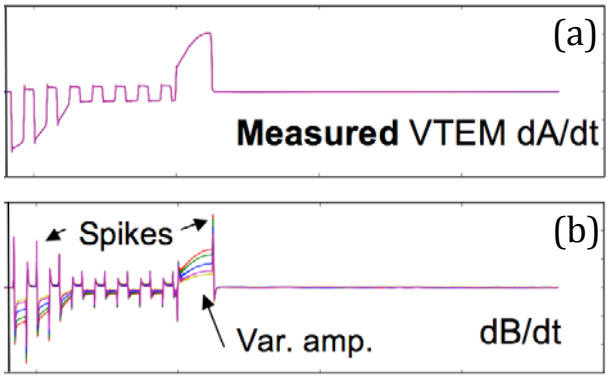

Figure 2: (a) Plot of overlapping 5 high-altitude waveforms with rate of change of current (dA/dt) measured at the transmitter and (b) corresponding received high-altitude induction coil (dB/dt) response. All 5 dA/dt waveforms have essentially identical amplitude and shape. The received dB/dt waveforms have a variable amplitude copy of dA/dt due to small changes in bucking geometry. In addition, there are additional spikes seen in dB/dt coincident with each rapid change in dA/dt. These spikes are the effects of distributed parasitic capacitance in parallel with loop inductance. (after Macnae and Baron-Hay, 2010).

There are several distinct categories of noise affecting AEM systems. Noise may be classified as stationary when its spectral characteristics are time (and for airborne systems location) invariant. Wideband, stationary noise can be reduced through averaging or stacking processes, and filtering can reduce this noise if outside the frequencies of geophysical interest. However, most noise sources are not stationary, and processing methods need to adapt to this to be effective. Some processing schemes adapt to spatial variations in noise (Schamper et al., 2012, Slattery and Andriashek, 2012, Wang et al., 2015) but these adaptive schemes including up to 6 or 8 seconds of averaging have unintended but significant negative consequences on anomaly interpretation as discussed later in this paper.

Figure 3 presents a compilation spectral plot of signals and noise collected in several different AEM systems in flight, and identifies the spectral characteristics of different signal and noise sources.

The ARMIT sensor internal noise (dashed red line) used in the BIPTEM system is shown on Figure 3, but this internal noise is negligible compared to other unwanted signals such as rotation in the earth's field (EF) that dominates at low frequencies. The EF noise is almost identical for the airborne HT SQUID and ARMIT sensors below 10 Hz, with the floating sphere University of Western Australia (UWA) suspension slightly better and the proprietary Geotem suspension somewhat worse. The BIPTEM sensor mount has suspension resonances (SR) below 1 Hz. Above 10 kHz, the ARMIT sensor detects unwanted signals from VLF, rotation rate sensors (22 to 24 Hz), the fluxgates (16 kHz), and noise from computer and other systems in the helicopter located 45 m above the bird. The smooth "bump" seen around 10 kHz is sferic noise, far more evident on the dB/dt sensor data (not shown). Only above 10 kHz is the observed noise spectrum limited by ARMIT sensor internal noise! No high frequency (> 1 kHz) spectra were published for the UWA, Geotem and SQUID suspensions and sensors.

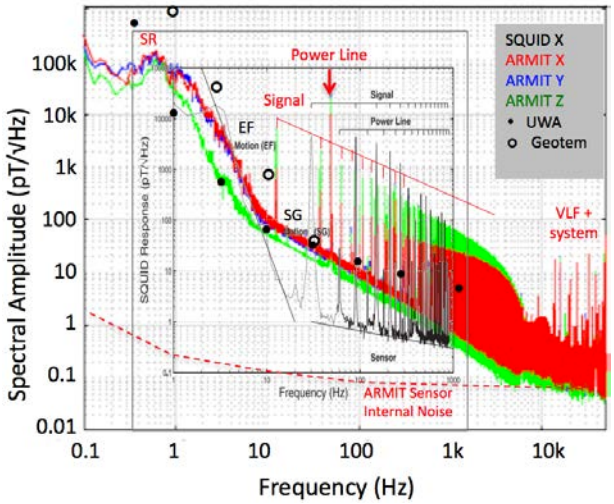

Figure 3: Amplitude spectra from AEM surveys. The sub 1 kHz black spectrum in Figure 3 is that from the x component of an airborne 30 Hz HT SQUID test in Canada as reported by Lee et al. (2001). It has 5 constituents: 60 Hz powerline fundamental and harmonics, 30 Hz harmonics for the transmitter signals, sensor internal noise, rotation in the EF noise and system geometry (SG) noise. Coloured spectra are three components from a 12.5 Hz BIPTEM airborne test in NSW, Australia. The powerline fundamental frequency is 50 Hz in Australia. Red annotations on the plot are for the BIPTEM system (Macnae et al., 2017) with an ARMIT (Macnae and Hennessy, 2017) sensor. Black dots are spot values of spectral noise detected by a Geotem sensor with the UWA rotation isolator and open circles are estimates for the original Geotem suspension predicted from a published dB/dt and rotation rate spectrum (Sunderland et al., 2017).

Natural Noise

Natural noise sources above 7 Hz in the AEM bandwidth are predominantly lightning strikes or sferics. Below 7 Hz, natural noise comes from ionospheric sources caused by changes to the solar wind source fluctuations and the effect on magnetospheric current directions caused by the earth's rotation.

Sferic signals are the source of energy for the airborne ZTEM system, collecting useful natural field data in the 20 Hz to 1 kHz range. Rather than being used as signals, controlled source AEM treats sferics as noise, and a sample along line Ex electric field time series for 0.25 seconds of sferics is shown in Figure 4. No AEM systems make use of such lightning location data at present, but this is likely to be an avenue of ongoing research.

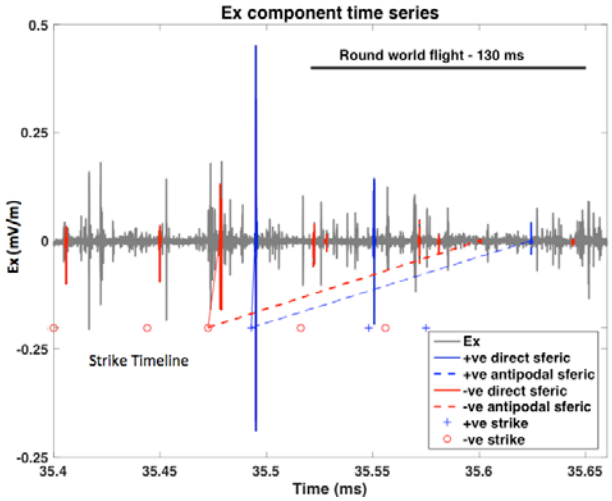

Figure 4: 0.25 seconds of streamed sferic data. The strike time of several sferics derived from the Vaisala detection network is shown with coloured symbols below the zero-amplitude axis. For the largest two source moments, both direct path and much smaller amplitude antipodal path sferics are detected. Figure modified from Hennessy and Macnae (2015).

Many EM data acquisition systems using off-time data "reject" sferics whose amplitudes lie above a threshold, either by a) clipping to a preset limit or b) removing 1 ms or so of sferic affected data. Option a) tends to bias data as there are more negative than positive sferics and the initial amplitudes are most likely to be clipped. Option b) creates an issue in that the missing 1 ms of data needs to be "sensibly replaced" if data is used in simple stacking processes, particularly those where stacking is intended to remove powerline harmonics. One suggestion in the literature is to use a remote reference to predict and subtract sferics from airborne data (Buselli et al., 1998) but this has not been implemented in airborne systems perhaps because of logistical and cost considerations, coupled with unknown speed of light time-delays depending on the direction of travel of the sferic.

The exceptions that use references are airborne ZTEM and ground magnetotelluric systems, where remote references are used for frequencies below 1 kHz where variable time-differences of less than 30 μs would occur for a reference base station within 10 km. Nyboe and Sørensen (2012) suggested that on the ground, the most important function of a local reference is identification of the frequency content of local noise sources to assist with waveform and window selection. Other than ZTEM, no other airborne borehole or ground systems claim to make much use of local or remote references. Practical local and remote referencing may well be a methodology that will see significant development in the next decade.

Cultural Noise

There are several sources of cultural signals, or cultural noise from a controlled source EM perspective, the main two being powerline currents at low frequencies and submarine VLF communications at high frequencies. As well as powerline noise, predominantly at 50 or 60 Hz and harmonics, low frequency noise is generated by many electrified railway systems, often at distinct frequencies such as 25 or 16.67 Hz. Switch mode regulators used for efficiency of transport systems often make these cultural signals wide-band and non-stationary as trains accelerate, decelerate and move closer to or further from a survey site. Powerline noise tends to be very constant in terms of base frequency, but its amplitude and the relative amplitude of harmonics often vary. The historic minimization of powerline noise through choice of a base-frequency whose harmonics interleave with the powerline harmonics is successful, and no changes to this strategy have occurred this century.

At high frequencies, the "unwanted VLF signals" consist of modulated transmissions around a central frequency. The power of these military transmitters frequently varies, and modulation systems and central frequency change from time to time. A discussion of how such signals may be accurately decoded and removed from AEM data was presented by Macnae (2015). I am however not aware of any implementations of this algorithm in commercial processing of ground or airborne data.

There are of course some systems which use the VLF signals directly for geophysical exploration and mapping. The exact details of how commercial AEM systems address the issue of VLF as noise is generally confidential. The simplest method of VLF signal reduction is to lower the high-cut frequency of the system. If a filter cuts the upper band to say 15 kHz, generally the resulting data is unusable at delay times before about 50 μs. Narrow-band filters aimed to remove one VLF station have undesirable side-effects causing severe ringing when used on data containing the sharp transitions typical of TEM waveforms (Macnae, 2015). Other methods attempt to make small adjustments in the system base frequency so that the centre frequency of strongest VLF station lies in a frequency notch of the transmitter spectrum. With actual VLF transmitter frequencies modulated, this last approach is also imperfect.

System and Geometry Noise

The first component of system noise is the internal noise floor of the sensor itself and other elements of an EM system also create some noise due to current flow in the various electronic and power supply components. As shown in Figure 3 however, sensor noise is often insignificant in the airborne case.

Geometry changes (sensor and transmitter rotations and relative locations) affect the observed response and create noise such as the SG noise shown in Figure 3 (Lee et al., 2001). Several methods have been published to address this problem, including the use of multiple GPS to measure rotations (Davis et al., 2009, Smiarowski and Macnae, 2013), pitch and roll measurement during survey (Auken et al., 2009), and using on-time field data to estimate changes in Tx-Rx coupling (Vrbancich and Smith, 2005; Smiarowski and Miles, 2015). Many commercial systems use "compensation", where empirically determined correction factors are applied to data based on high altitude data, where observed primary field amplitude in the various components is measured during manoeuvres. Corrections using either compensation or geometrical monitoring and prediction are then applied to data, which corrections have steadily improved over the past two decades.

Time domain system waveforms have varied considerably over the years. The first such waveform was the fixed-wing Input alternating half-sinusoid with a nominal interspersed off-time (Fountain, 1998). While the transmitter current may have been off, the large currents induced in the aircraft slowly decayed, and the receiver that detected these only had an "off-time" in marketing material and compensated data. Imperfect removal of aircraft response is not a major source of noise however at present.

Sensor internal and electronic noise reductions, with high-frequency isolation systems from sensor vibration have made for an order of magnitude reduction in noise for the VTEM system in the two decades to date (Kuzmin and Morrison, 2008; Combrinck, 2010). Other helicopter AEM systems have made similar reductions in noise levels (SkyTEM, 2014).

Rotation Noise

One thorny problem is that of rotation noise, sometimes called motion noise, which is caused by rotations of the EM sensor in the earth's magnetic field. These cause a change in magnetic flux cutting through the loop or along the axis of the sensor. If the angle between the sensor component direction and the EF is $\theta + \phi\sin(\omega_0 t)$ for simple oscillation of amplitude ϕ at angular frequency ω_0, then signals are induced in the sensor of the form $\cos\theta\sin(2\omega_0 t) + \sin\theta\sin(\omega_0 t)$, i.e. at both the frequency of oscillation and double this frequency (Kratzer and Macnae, 2013). The doubled frequency component is generally smaller and affects measured sensor components sub-parallel to the EF. The components of B or dB/dt perpendicular to the EF are most affected by rotation noise (Munkholm, 1997).

Rotation noise is the prime reason that AEM systems have been limited in base frequency to 25 or 30 Hz. Ground systems easily collect data at 1 Hz or lower base frequencies, using lower power transmitters and similar sensors. While airborne data have historically been collected at lower base frequencies than 25 Hz, prior to the year 2016 such data were of very poor quality (Vrbancich et al., 2005). Major efforts by virtually every airborne contractor and to my knowledge two mining companies have been undertaken in the past attempting to improve suspension systems and minimize unwanted rotations. The many failures and the approaches taken mostly remain confidential. Several approaches to rotation minimization have resulted in patent disclosures by BHP Billiton, Vale, CGG, and Fugro. One recent paper discusses the reduction in rotation noise using the UWA suspension system (Sunderland et al., 2017). Only last year was the first apparently useful 15 Hz and 7.5 Hz low frequency component data published by Konieczny et al. (2016). Insufficient survey results have been published at the time of writing to determine if any of these methods have provided a real breakthrough that can be routinely flown at low enough noise to be useful.

One potential methodology to correct for rotation effects is to directly measure these rotations, and then predict the expected effect on every component of the magnetic or dB/dt sensor (Kratzer and Macnae, 2013). This method has been implemented in the BIPTEM system and will be discussed later in the paper. There is emerging evidence of a breakthrough in rotation noise minimization and correction, but only extensive field testing in the next year or two will show if this is the case.

Total field magnetometers have been used with large loops and / or grounded bipoles in the HeliSAM system, based on the ground method of Cattach et al. (1993). Total field data are free from rotation noise. Total field anomalies, however, are bandwidth limited to a few kHz at best, have higher sensor noise levels than other sensors, and measure the anomalous component projected onto the EF. That is, HeliSAM will only be able to measure relatively late delay time data for a specific and unalterable component; that component ranging from horizontal due North at the magnetic equator to being vertical at the magnetic poles. Such data can however be useful (Yang and Oldenburg, 2016) in the detection of highly conductive sulphides.

2: SIGNAL ENHANCEMENT

Many choices need to be made in AEM transmitter design. Frequency or time domain? Bandwidth? Off-time or All-time acquisition? Relative lengths of off- and on-time? Single or multiple transmitters? Simple or complex waveform? Data windowing for compression and noise reduction? Bucked or unbucked? Generally, it is a good idea to maximize signal, remembering that it is the product of peak dipole moment with transmitter on-time duration that is the best measure of signal, but there are many constraints and trade-offs to be considered, such as available power, whether aircraft-sourced or generated independently, maximum weight for a given helicopter, safety, loop size, and stability. Large dipole moments generally require distant sensors (e.g. fixed-wing geometry), active primary field bucking at the receiver (Chen et al., 2016) or orientation of vector sensor receiver perpendicular to the primary field (Sørensen and Auken, 2001). With aircraft operating costs increasing greatly with increases in size and power, limited advancements have occurred in the last decade, no significant increases are expected in sustained dipole moment in the next decade unless large airships become economic to operate.

Since this is a paper on processing advances, I will gloss over any comparison of time or frequency domain systems. Frequency domain processing has not changed much in the last decade, and has been very well covered by Valleau (2000). Frequency domain mapping is at present preferable for high-resolution very shallow mapping as it makes use of phase referencing at high frequencies. One degree of phase resolvable at 100 kHz is equivalent to a time delay of only 27 ns, a delay far shorter than any attempted in airborne time domain EM, measuring a response more in the range of ground GPR systems. Commercially available time-domain shallow-sounding such as the low-moment SkyTEM system collects data with delays from a few μs, and is the best of the commercial time domain systems for very shallow sounding in conductive areas where the induced current stays near surface. If, however, the system is operated in dual moment mode, low moment data only collect soundings every second (~30 m) or so, with the intervening data filled by interpolation.

Bandwidth

Deeper penetration requires more power, longer delay times, and equivalently lower base frequency. The lowest usable airborne frequency is set by rotation noise, historically 25 or 30 Hz, depending on the powerline frequency. If very shallow sounding is of interest, then the system must collect very early delay time data, necessitating sensitivity at high frequencies (many 10's of kHz). This in practice requires either measurement during the transmitter turnoff or just after. However, all early delay times are affected by residual transmitter currents from parasitic capacitance effects (Macnae and Baron-Hay, 2010; Schamper et al., 2014). The nature of parasitic capacitance and its effects on signal (e.g. Figure 2) are not well documented and usually ignored in the geophysical literature. Corrections to measurements taken in the turn-off ramp and at very early times after turn-off can be applied using frequency domain deconvolution which is affected by Gibbs phenomenon near the Nyquist frequency, or empirically with exponential fitting (Schamper et al., 2014). In the wideband systems necessary to collect very early delay time data, there are severe processing issues, particularly within a few hundred km of strong VLF transmitters used in submarine communications.

Given a specific base frequency limits the lowest usable frequency, there are three ways in practice by which wideband data (a wide range of delay times from very early to very late) can be collected. These are a) deconvolution of streamed data; b) composite waveforms; and c) multiple systems with different base frequencies. Each has advantages and disadvantages, described briefly below.

Deconvolution / Compensation

The highest resolvable frequency in sampled data is set at the Nyquist frequency, half the sampling rate of the streamed data. Sampling rates are now commonly more than 150 kHz, whereas in 2007 systems used much lower sampling frequencies less than 100 kHz. Deconvolution processing was first described by Annan (1986) for the Prospect 1 AEM system and has been described in more detail by Lane et al. (2000) for Tempest and by Macnae and Baron-Hay (2010). Key to the deconvolution approach is availability of linear data, specifically data where the digital output is linearly proportional to the field being measured. This requires (slightly) oversampled data unaffected by electronic slew-rate and other issues such as clipping, for both the transmitted current and the received waveform, as well as very high altitude data to use as a reference. Spectrem and Tempest fixed-wing AEM systems have used deconvolution successfully for decades, providing quantitative square-wave response data from very early delay times, as low as 13 μs for Tempest.

Compensation based on straight and level flight and manoeuvres at high altitude can at times provide corrections to data comparable to those achieved by deconvolution. Compensations methods for magnetics are well described in the literature (e.g. Groom et al., 2004), and have been adapted for AEM in proprietary codes by most airborne contractors. Figure 5 is an example from the Oban area in Canada of compensated, wideband VTEM data in the off-time which has been transformed in Geotech standard processing to apparent resistivity. In 2007, the earliest useful delay times were around 0.13 ms, nearly a decade later in delay time.

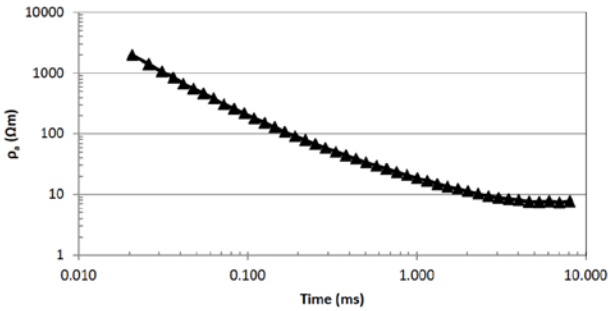

Figure 5: Example of Canadian VTEM data converted to apparent resistivity with consistent response from early (20 μs) to late (8 ms) delay times. The accuracy at early delay times is the result of improved compensation methods.

Composite waveforms

An example of a composite waveform and its spectrum introduced by CGG is shown in Figure 6. This waveform comprises a large amplitude pulse followed by a long off-time to recover deep information, combined with a smaller amplitude, steep-sided pulse and short off-time to produce good short-delay time data. The turn-off time of the small amplitude pulse is short enough to be approximated as a step. Published data show significant improvements in conductivity-depth resolution for materials with resistivities in the 10 to 50 Ωm range (Chen et al., 2015).

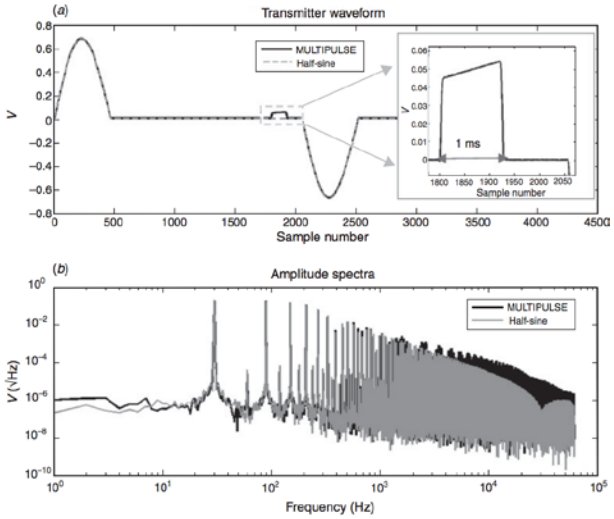

Figure 6: (a) MULTIPULSE (composite) and half-sine transmitter waveforms and (b) their amplitude spectra derived using the FFT of 1 s sample of raw streamed data. The insert shows the zoomed-in view of the trapezoid pulse. Figure from Chen et al (2015).

Other examples of composite waveforms in use in geophysics are pseudo-random binary sequences (PRBS), which have been successfully employed in marine environments (Ziolkowski et al, 2011) and in Russian ground EM systems (Velikin and

Velikin, 2016). No reported AEM tests of PRBS waveforms were found in a literature search.

Multiple System (Dual moment)

Most frequency domain systems are multiple, with one tuned Tx-Rx pair per frequency. These pairs independently require frequent calibration (Valleau, 2000; Ley-Cooper and Macnae, 2007) to ensure consistency with each other and measurable physical properties. In time domain where shallow data is important, SkyTEM (Foged et al, 2013) generally alternates between two transmitters: a single or double turn, small current system with rapid turnoff operating at high frequency and a multiturn, high current system with longer turnoff operating at a lower base frequency. Due to loop inductance and to a lesser extent parasitic capacitance considerations, the small moment single turn system has a much higher slew-rate and faster turn-off than a multiturn, high current system.

Dual moment systems increase bandwidth, which can allow for good early time data, particularly useful in shallow conductor mapping. The systems can suffer from various problems: 1) systems alternate so each has "gaps" in its data later filled by interpolation and 2) the overlap in response of the low and high moment systems has very different signal to noise ratios. In SkyTEMFast, for example, the ratio of dipole moments (and hence intrinsic noise) is a factor of 460,000 to 3000; or about 138:1, with a respective share of system time in the ratio of about 3:1. The low moment data will be a significant factor (~70 times) noisier at the same delay time window, since the low moment data has about 4 times the number of stacks in each measured interval. An example with observed data in Canada is shown in Figure 7. Where the near surface is conductive (Figure 7, decay B) and where the EM decay has not penetrated too far into the ground at the early delays, the low and high moment SkyTEM responses roughly "overlap", collecting good data over a wide range of delay times. In terrains with a resistive near-surface layer, the low-moment response may be mostly in the noise, and not overlap with the high moment response (Figure 7, decays A). There can be a decade of missing delay times where no valid data or apparent resistivity can be obtained.

Figure 7 example data were collected from a survey area where the SkyTEMFast and VTEM lines were interleaved, 100 m apart. The values above noise are connected with bold lines. Responses below 0.01 pV/Am^4 in amplitude have been clipped for plotting on the log scale. The slow decay from a deep conductor is clearly mapped in the high moment SkyTEM A and VTEM data, but only the first two points of the low moment SkyTEM A response are above noise. These two low moment points above noise probably reflect the response of very slightly conductive surface overburden, not detected by VTEM. These example decays are typical of the survey data in this area with resistive near-surface materials. SkyTEM decay B is from a more conductive area some distance away, with a large response from early to late delay times showing the commonly expected overlap in responses. Other variants of SkyTEM collect high-moment data to earlier delay times, with lower noise levels, so Figure 7 results should not be regarded as typical.

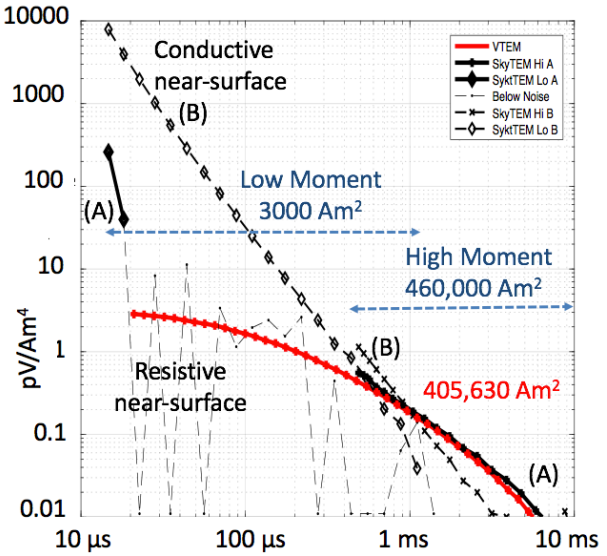

Figure 7: Example measured decays in delivered data from 2016 SkyTEMFast and VTEMplus mineral exploration surveys in Canada. The VTEM and SkyTEM A responses come from a resistive area with a deep conductor. The SkyTEM B decay is some distance away in an area with thick conductive sediments present.

At this site, the dual moment SkyTEM provides a limited advantage at the two very earliest delays, at the expense of a poorer characterization of the deep conductor where the low moment data had insufficient dipole moment to provide data above the noise level over a decade in time.

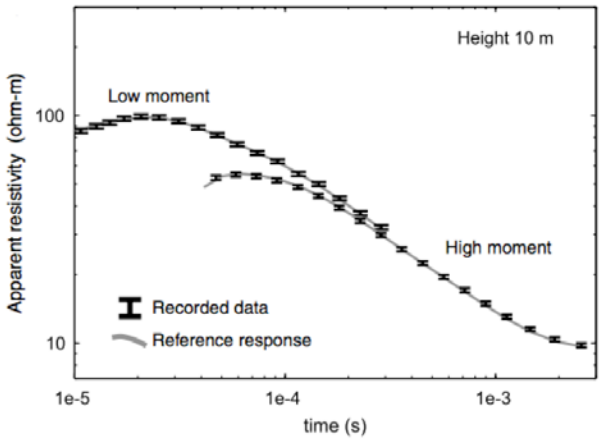

Figure 8: In conductive terrain, such as the Lyngby test site in Denmark, dual moment systems usually produce overlapping estimates of apparent resistivity. (Figure from Foged et al., 2013).

Slight inconsistency between the high and low moment system responses (Figure 8) and their interspersed sounding locations makes data processing and modelling more challenging than that required for single moment systems, due to factors such as independent system drift, much as was the case for frequency domain multicoil systems (Valleau, 2000). The effects of

waveform periodicity cause the variable amplitude gap between the high and low moment systems.

3: SUPERPARAMAGNETIC EFFECTS

Superparamagnetic or viscous magnetic effects arise primarily from single domain magnetic minerals whose dimensions are less than 1 μm. Such fine grained minerals in soils may arise from bushfire oxidation of goethite or from the secretions of Gallionella bacteria, while in rocks they may arise in volcanic glasses, tuffs, or as a byproduct of shearing and breakup of larger grains (Gaucher and Smith, 2017). Lee (1984) introduced a simple mathematical model for SPM effects in time domain EM, based directly on the work of Chikazumi (Chikazumi and Charap, 1978). This model explained unusually slow, small amplitude decays in ground coincident loop Sirotem data, initially interpreted to be deep conductors. A "field solution" to this problem was to separate the transmitter and receiver loops by a distance of a few metres, which generally eliminated the detection of these SPM signals.

Much to the surprise of many ground geophysicists with experience in eliminating SPM by moving receiver loops a metre or two away from transmitter loop wires, AEM systems in Africa detected small amplitude SPM decays. SPM was only recognized as such in the airborne data by Paul Mutton after several unsuccessful holes were drilled to intersect the assumed buried source of slowly decaying anomalies. With collaborators (Kratzer, et al., 2013; Sattel and Mutton, 2013) and with design of a ground testing system, these slow AEM decays were proven to be surficial SPM in origin even with the AEM system at altitudes over 40 m above ground.

When subjected to the magnetic field from an EM transmitter, the demagnetization of SPM particles in a 10-cm thick layer of diameter 100 m reduces the anomalous vertical magnetic field by a factor of about 1000 (Tarasov, 1938, Skomski et al., 2007). Thus, for vertical primary fields there is virtually no effect from the SPM layer (Kozhevnikov and Antonov, 2011). For horizontal magnetic fields, demagnetization is negligible in the layer, so magnetic fields are magnified by the SPM susceptibility.

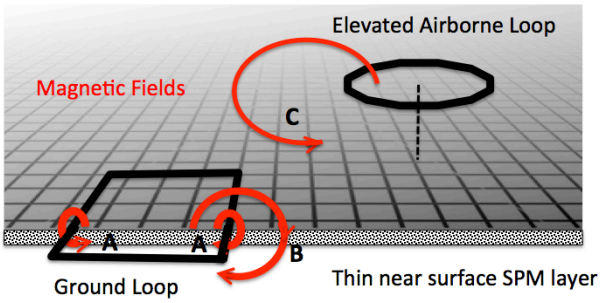

Figure 9: Schematic image of ground and airborne loops over a thin SPM layer.

Figure 9 shows schematically that the primary magnetic field of a ground loop is horizontal in the near-surface thin layer under the ground transmitter for only a very short distance at A, while the field from an airborne loop is horizontal for a longer distance at C around the AEM transmitter loop. At any distance, such as at point B away from the ground loop, the local primary field is sub-vertical, and SPM effects will be negligible due to demagnetization.

Thus, in concept, ground loops primarily energize a shallow layer of SPM only directly under their wires, with demagnetization virtually eliminating detectable SPM effects at any reasonable distance from the transmitter loop. On the other hand, AEM primary fields are sub-horizontal for a considerable distance in a ring around the AEM loop, and the SPM effect can be detectable as the magnetic layer geometry does not lead to significantly demagnetization from this primary field geometry.

In data, SPM can be recognized through several methods: For a step-off of transmitter current a) it has approximately a log(t) (step response or B field) or a $1/t^{1+\alpha}$ (dB/dt impulse response, with $-0.4<\alpha<1.4$) decay at late delay times. For shallow sources expected in regolith b) its spatial variations are too rapid to come from a deep target (Macnae, 2016) or c) its vertical gradient is high (Sattel and Mutton, 2014). The vertical gradient method requires either two receivers at different heights on one AEM system, or repeat flights at two different altitudes.

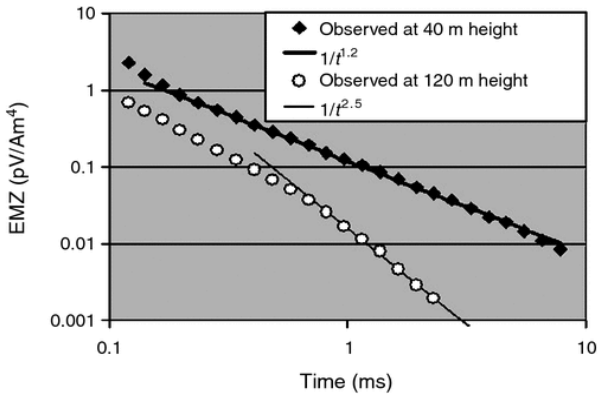

Figure 10: VTEM decay response recorded 40 m and 120 m above SPM material with time dependences of $t^{-1.2}$ (SPM) and $t^{-2.5}$ (conductive half-space) indicated. Figure from Sattel and Mutton, (2015).

Figure 10 shows typical VTEM decays from Africa (Sattel and Mutton, 2015). At 120 m altitude, the late-time data exhibits the $t^{-2.5}$ decay expected from a halfspace, whereas it exhibits a $t^{-1.2}$ decay characteristic of SPM at 40 m system altitude.

Chikazumi and Charap (1978) showed that for a collection of SPM grains with a uniform distribution of time constants between two widely-spaced limits, the impulse response should be of the form 1/t. The variations in decay of SPM responses (empirically characterized with parameter α) can be explained with changes to the size distribution. The relaxation time constant τ_N of a single domain magnetised SPM grain is given by the Néel (1949) equation to be:

$$\tau_N = \tau_0 \exp\left(\frac{KV}{k_B T}\right), \qquad (1)$$

where τ_0 is the attempt time (material dependent, usually less than 1 ns), KV is the height of the energy barrier, a product of particle volume V and material dependent anisotropic magnetic energy density K, T is absolute temperature and k_B is Boltzmann's constant. A narrow range of particle sizes will thus lead to a wide range of Néel time constants, thanks to the exponential term in Equation (1). An EM excitation will then allow detection of a composite decay drawn from many time constants.

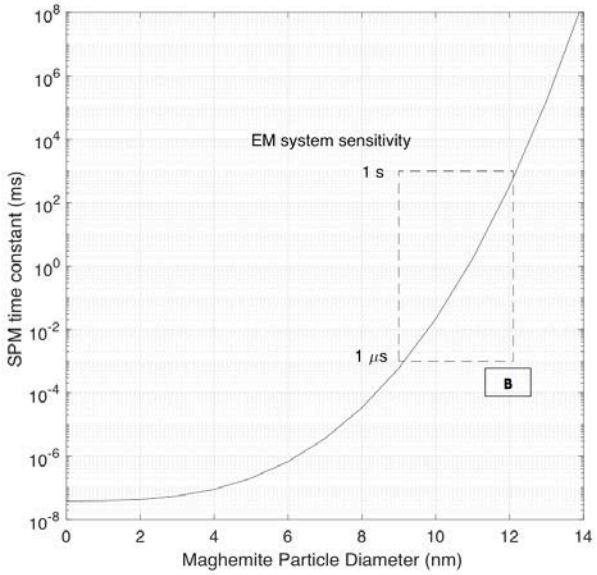

Figure 11: Néel (SPM) time constant as a function of laboratory maghemite particle diameter. An EM system with sensitivity to exponential decays in the 1 μs to 1 s range will only sense responses from maghemite particles in the 9 to 12 nm diameter range! The horizontal extent of the box around symbol B shows measured diameter range of bushfire-generated maghemite after one major event (Grogan et al., 2003).

Using laboratory values for maghemite (Pisane et al., 2015) in Equation (1), I predict the values of the Néel time constant τ_N as a function of particle diameter and this is presented in Figure 11. Most geophysical EM systems operated at base frequencies in the 1 Hz to 100 Hz range are sensitive only to time constants in the 1 μs to 1 s range (Hodges and Chen, 2015). EM systems will thus only detect responses from a 9 to 12 nm range of laboratory, and by reasonable inference field, maghemite.

Numerical experiments have shown that if SPM particles have sizes towards the larger end of the sensitivity range, the observed SPM decay in a *dB/dt* system is slower than 1/t (α<1), whereas if SPM grains predominantly have time constants in the shorter end of the detectable range, the observed decay is faster than 1/t (α>1). Multidomain grains may also show small SPM effects, which could further complicate observed EM decays.

As already noted, SPM can be fitted to data during processing using a $1/t^{1+\alpha}$, where -0.4<α<0.4. However, the SPM effect is opposite in sign and very similar in shape to AIP, with the result that without constraints simple linear fitting may become unstable (Macnae, 2016b). The B field decay characteristics are quasi-logarithmic in nature for asymmetrically distributed grain sizes or τ_N values, and generally more difficult to numerically characterize than is the dB/dt decay.

4: AIRBORNE INDUCED POLARISATION

Conventional AEM

Inductive induced polarization (IIP) effects have long been recognized as occasionally being detected in airborne EM data. The first published case (Smith and Klein, 1996) of AIP was from the Arctic, and it is only recently that the mechanisms of strong IP effects of water in the permafrost have been understood and described in the literature (Stillman et al., 2010). AIP effects are regularly seen in Arctic environments where permafrost and high porosity coincide, such as in near-surface unconsolidated materials or kimberlites (Kang et al., 2017). With the significant reductions in system noise levels in the last decade, AIP has been shown to regularly and routinely affect measured late time data. Different research groups have used 1D and occasionally 3D models to understand and separate EM from IP effects in data (Goold et al., 2007; Hodges and Chen, 2014; Kwan et al, 2015; Macnae, 2016b; Kaminski and Viezzoli, 2017; Kang et al, 2017).

The inductive IP effect has been mathematically characterized with several models. Geophysically, the most common is the Cole-Cole model expressed either in conductivity or resistivity, with an inductive source that depends on both the AEM system and the 3D conductivity structure of the ground. The conductivity and resistivity models have three essentially identical parameters, a high (or low) frequency limit conductivity or resistivity, a chargeability m, and a frequency dependence c. The fourth parameter, a time constant τ, is different between the two formulations, related by an expression derived by Tarasov and Titov (2013) with discussion by Macnae, namely:

$$\tau_C = \tau_R (1-m)^{1/c}, \qquad (2)$$

where subscripts C, R refer to the resistivity and conductivity Cole-Cole formulations respectively.

The Wong (1979) electrochemical model suggested that c = 1 (the Debye model) was best for charge separation models without chemical reactions, whereas c = 0.5 (the Warburg model) was best for ionic fluid-sulphide reactions where diffusion of ions altered the response near the electronic (sulphide) interfaces. Pelton et al (1976), found that in many sulphide deposits, the values of c around 0.3 or lower best fit observed sulphide data, implying a range of grain sizes were present in the deposits tested.

As well as using the product (in frequency domain) of two or more Cole-Cole responses to characterize data with complex behavior, there are two other decompositions of IP responses

presented in the literature. These are the distributed Debye (DD) and the distributed Warburg (DW) decompositions. DD fits a distribution of Debye decays with different time constants to data. It has been extensively discussed in the literature by e.g. Nordsiek and Weller (2008) and was used by Marchant et al. (2014) to fit AEM data with AIP effects. DD fitting leads to composite estimates of m and τ (Weigand and Kemna, 2016).

Macnae (2015, 2016b) introduced the distributed Warburg decomposition to model AIP data, although he did not name it as such at the time. Based on ground modelling methodology, he fit a DD decomposition to the EM, and convolved this with a distributed Warburg decomposition (cDW) to fit any AIP data (Figure 12). The typical EM decay of an isolated conductor or layered earth can be accurately fit with a DD decomposition. Such EM responses however cannot be accurately fit with a DW decomposition as the EM decays are "too fast". While the jury is out on the best decompositions, the combined (DD + cDW) decomposition as described by Macnae (2016b) is well suited to separating IP decays of sulphides from EM, as DW basis functions cannot in practice fit the EM decays.

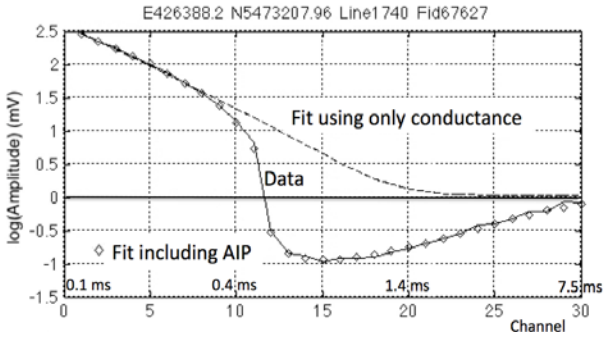

Figure 12: Example of a large AIP affected VTEM system decay, well fit by a combination of distributed Debye (to fit the AEM) and convolved distributed Warburg (to fit the AIP) decays (Macnae, 2016c).

Whether using direct Cole-Cole, distributed Debye or convolved distributed Warburg, sensitivity analyses show that parameters c and τ are poorly resolved, largely because AIP responses are confined to the tail-end of a very much larger EM decay. The AIP response above noise does not have sufficient bandwidth to fully characterize source parameters

From a mineral exploration perspective, away from permafrost, the first fundamental point to note in AIP is that airborne system base frequencies are more than two orders of magnitudes higher than those used in ground IP equipment. A consequence of this, predicted from physical property data and electrochemical models, is that AIP is sensitive to much finer grained metallic minerals than is ground IP (Macnae and Hine, 2016). There is some evidence that AIP may detect a "halo" that maps finer grained alteration around conventional IP targets. Some useful uranium mineralization associations have been reported by Babu et al. (2017), and titanium mapping associations by Macnae (2016c). On the ground, at lower base-frequencies, Flores and Ortega (2001) reported a close association of ground inductive IP with porphyry sulphides at El Arco. Clays may also produce detectable IP anomalies from airborne EM transmitters (Kolaj and Smith, 2013), useful in mine tailings mapping.

Perhaps, the most useful consequence of the recent AIP modelling and inversion studies is that by separating AIP and AEM effects, conductivity-depth imaging or 1D constrained inversions using Cole-Cole models produce much better conductivity maps in IP affected areas (Macnae, 2016c; Kaminski and Viezzoli, 2017). Figure 13 is an example of separate resistivity and chargeability mapping.

Because of the slowly decaying nature of AIP responses, simple mathematical modelling suggests that B field sensors would be more sensitive to AIP than dB/dt sensors. Exactly as has been the case for good conductor detection under cover (Asten and Duncan, 2012), the AIP response should appear much earlier in delay time with a B than a dB/dt sensor.

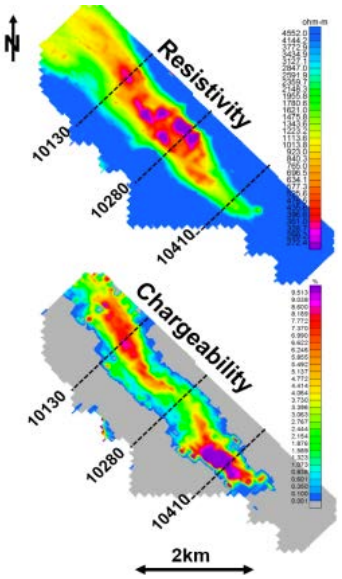

Figure 13: Example of resistivity and chargeability fitted to HELITEM data. Figure from Hodges and Chen, 2014, using data courtesy of Triple 9 resources. Note the coherent but spatially distinct mapping of apparent chargeability within the conductive zone.

Airborne B field IP: BIPTEM

There has long been a desire to record "good" IP data from an airborne platform. Three major mining companies conducted proprietary feasibility studies using internal physical property models and computer modelling in the 2000s, all of which suggested that AIP might be feasible. Different studies investigated different options using different software. Common from the modelling was: a) a need for as low a base frequency as possible, implying a preference for a B field sensor; b) a preference for a >200 m transmitter-receiver separation; and c) a recognition that signals were large enough to be detected if motion noise could be reduced to a few pT.

Independently, Macnae performed modelling which revealed that the airborne secondary electric field was significantly more sensitive to AIP than the magnetic B or dB/dt fields. AMIRA projects P1036 and 1036a initially developed a non-contacting charge-coupled capacitive electric field sensor (En5c) with ~10 nV/m sensitivity. This sensor performed superbly in a Faraday cage, but was rendered useless in the field by ambient noise. This noise consisted of a) variations in the earth's vertical electric field (typically +100 V/m, but ranging from -100 to +300 V/m;), and b) charge on wind-blown dust as noise levels

were strongly related to wind velocity. This airborne charge arises from many sources including charged dust, ground radioactivity, and animals and humans who each shed over 10 million microscopic charged squamae (pieces of skin which are dust-mite food) per day.

In 2016, Thomson Aviation and Monex Geoscope conducted a number of airborne tests of a combined airborne B and dB/dt field sensor to complete the originally planned work in AMIRA project P1036a. Using a 1000 m by 400 m transmitter loop on the ground, experimental AEM and AIP data were collected over the Lewis Ponds deposit, New South Wales using a suspended ARMIT induction magnetometer (Macnae and Hennessy, 2017) measuring streamed B, dB/dt and rotation rate (Jaroszewicz et al., 2016) data with a Terrascope 12-channel, 24-bit data acquisition system. A previous VTEM survey had detected AIP effects displaced to the east from peak ground IP chargeability responses coincident with the deposits (Hine and Macnae, 2016). Initial analysis shows that clear AIP effects were detected in 12.5 Hz B and dB/dt field data.

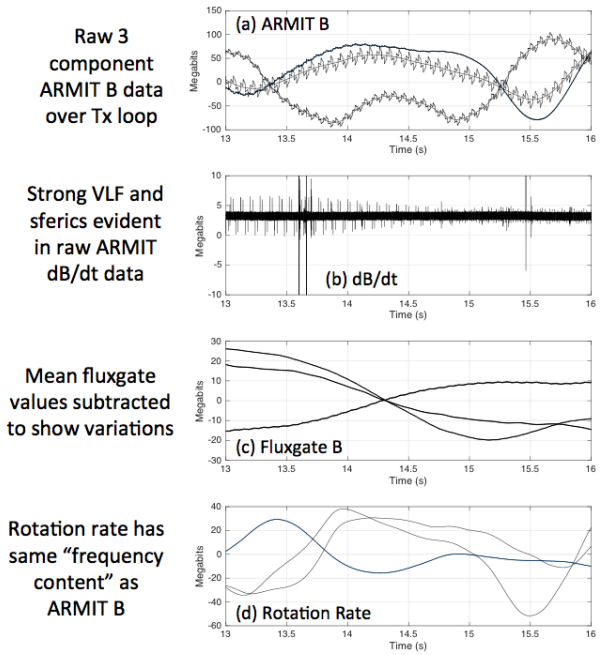

Figure 14: Example of 3 seconds of BIPTEM data at Lewis Ponds.

Figure 14 shows a sample of raw BIPTEM data recorded over the transmitter loop. A large, low frequency background variation is clearly evident in (a), superimposed on the 12.5 Hz B field data from the transmitter. The wavelengths of this background are similar to those in the rotation rate data (d). Rotation rates were measured with a non-conductive, non-magnetic rotational seismometer (Jaroszewicz et al., 2016). This observation empirically confirms that the low-frequency B field background response is predominantly caused by rotations in the EF. The raw dB/dt data (Figure 14b) is dominated by high-frequency sources: the "thick black" stripe along the zero-amplitude dB/dt axis is the combination of several distant (3000 km + to source) VLF signals. The consistent alternating double spikes are produced by the bipolar transmitter waveform, switching on and off. The decrease in amplitude to the right occurs as the receiver moves away from the transmitter. Big sferic spikes are seen around 13.6, 13.7 and 15.4 seconds on the dB/dt plot, with many more smaller spikes evident on close inspection, particularly on an expanded plot.

There are many steps required to extract AIP responses from raw data such as that shown in Figure 14. These include the basic AEM processing steps including the separation of primary and secondary fields, prediction and subtraction of low-frequency rotation noise, sferic spike and VLF removal, sensor frequency response correction, stacking and windowing. A subsequent step is the fitting of AIP decays to observed data to predict apparent chargeability, and if possible, other apparent Cole-Cole parameters. This simple fitting allows for the separation of AIP responses from AEM in this data as has been discussed for conventional systems.

With much easier operational and suspension constraints than SQUIDS, it is expected that B field measured systems using moving transmitters and inductive magnetometers will become commercially available and more common over the next decade.

5: CALIBRATION AND QC

There are good calibration methods to ensure that the physical parameters of system geometry, receiver and transmitter Voltage and Amperage waveforms are correctly and accurately measured. This, while conceptually sufficient, however is not quite enough to calibrate an AEM system in practice. Received waveforms are affected by sensor and system bandwidth, problems with variable bucking and parasitic capacitance (previously shown in Figure 2), and stray responses from aircraft when the transmitter loop is mounted on the airframe or too close to it. As system noise has decreased in the past decade by an order of magnitude or so (Combrinck, 2010, SkyTEM and Geotech websites), and dipole moments have increased in many systems, the 30 or 40 m tow-rope that once was "far enough" has now often become "too close".

Good high altitude data, with accurate voltage measurements to obtain the transfer function from Tx to Rx can reasonably characterize a linear system, although changing system geometry and temperature controlled electronic drift during survey introduces complications. However, to completely escape from the earth's detectable response, high altitude may need to be 2.5 km or more over some conductivity structures, never routinely achieved in production surveys as this height is uneconomical (it would take too much time and cost to climb this high, at times into regulated airspace, and essential visibility can be lost if a cloud ceiling is present) or even impossible to achieve. A second approach to overcome physical calibration difficulties was introduced by the Aarhus group, with Danish government support: a physical test site was established at Lyngby. After flying a stable system over the reasonably 1D site, two "fudge factors", specifically an amplitude scaling and a time-shift can usually be derived to achieve some consistency between inversions of the "calibrated" data and the preferred conductivity model (Foged et al., 2013).

This preferred conductivity model has been refined from time to time. Rainfall and groundwater diffusion history is however likely to have some effect on the near surface conductivity on occasion, so the preferred model cannot realistically be taken to be an exact standard. Consistency checking at well-known and documented sites is undoubtedly very useful. At Lyngby, the fitted time-shift can identify time delays cause by finite AEM system bandwidth that are not always consistently corrected, and the fitted amplitude may help estimate an unknown primary field amplitude if an AEM system does not have a current monitor and or can only be operated in bucked mode. Sites such as Lyngby have provided essential information on AEM systems for hydro-geophysical conductivity mapping purposes. A consistency check for an AEM system over a 1D site is however insufficient for many mineral exploration surveys, as it does not measure the variable amount of frequently undocumented lateral averaging that may be applied to data.

Instrumented ground loops with AEM system overflight can accurately characterize both a system and can quantify any averaging in delivered data (Yin and Hodges, 2009; Davis and Macnae, 2008). Because current induced in the loop is measured and recorded during overflight, the response at the airborne receiver can be accurately predicted and compared to the contractor delivered data, exactly identifying and quantifying any lateral averaging. They are an excellent calibration method that has not however become standard in the industry. Instead, a number of small uneconomic sulphide targets have been used for comparison of AEM system lateral resolution and noise level: examples being, Reid-Mahaffey and Caber in Canada; Forrestania and Valen in Australia. It is always difficult to compare "current" AEM systems, as competing systems have often improved since the last publically available test at a test site, and sferic noise and turbulence (motion noise) tends to be worse in summer than in winter.

There are many variants of AEM systems given the same generic name, each of which may have quite different signal and noise characteristics. It is often difficult to get comparative data from different systems operated by the same company, let alone comparative data of all available AEM systems. I will illustrate some of the issues in comparison of two specific systems with a historic example at the Valen test site, South Australia, where both VTEM and SkyTEM^{508} data were collected using different AEM systems in early 2013, and where CSIRO has made comparison data available. Effersø and Sørensen (2013) reported on this comparison on the SkyTEM website, and Eadie and Prikhodko, (2013) published an alternative analysis on the Geotech website. Both these analyses were available on the company websites in June 2017.

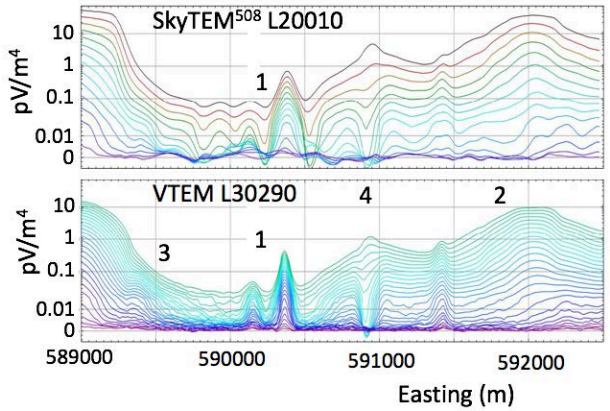

Figure 15: Comparison of VTEM and SkyTEM data along the same profile over several conductors at Valen, South Australia. Plotted are SkyTEM channels from 0.3 to 10.4 ms, and VTEM channels from 0.3 to 10.7 ms. Figure modified from Eadie and Prikhodko, (2013). Locations 1 to 4 are discussed in the text.

On one line presented (Figure 15) and other lines, at early and intermediate delay times, Effersø and Sørensen (2013) noted that VTEM amplitudes (both in equivalent pV/Am^4) were lower, which they reasonably attributed to SkyTEM's faster turnoff. However, their analysis did not appear to take into account the fact that VTEM data was collected on average at a higher altitude, which would have contributed to the observed difference. Effersø and Sørensen (2013) presented linear amplitude plots, and concluded that the two system consistently had equivalent late time noise levels, while Eadie and Prikhodko (2013) asserted on the appearance of linlog amplitude plots with greater visibility of small signals that VTEM noise was a factor of 2 to 5 lower.

Analysis of the "shortest significant wavelengths" in the delivered late-time data shows wavelengths between 30 and 40 m for VTEM and a little over 100 m for SkyTEM on the line shown in Figure 15. The VTEM data wavelength is consistent with a flight altitude of 35 m, and less than 1 second of proprietary averaging.

The SkyTEM processing manual (Aarhus University, 2011) and Schamper et al. (2012) discuss the use of trapezoidal averaging in standard SkyTEM processing, where narrow averaging windows are applied at early delays, but quite wide (>100 m, up to 300 m) and adaptive (noise driven) averaging windows are applied to data at late delay times. In this case, the observed smoother spatial variation of the SkyTEM data and the apparent wider response of anomalies at location 1 on Figure 15 appear to be consistent with SkyTEM published standard trapezoidal averaging. Figure 16 presents a schematic diagram of the trapezoidal windowing scheme.

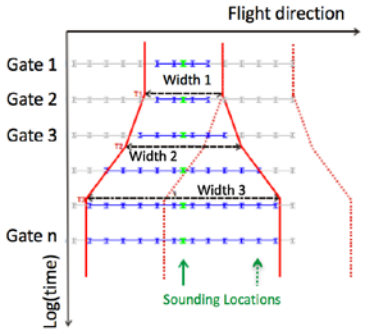

Figure 16: Schematic diagram of trapezoidal averaging of SkyTEM data (modified from Schamper et al., 2012). The width of the late time average can be fixed or noise-adaptive, or on request be kept the same for all channels.

On balance, at Valen, both VTEM and SkyTEM systems detected the same background and the same anomalous features, and both would be quite suitable for conductivity mapping and mineral exploration in this area. At marker 4 (59900E), both systems detect a response typical of a polarizable conductor, with amplitude enhancement at early delays and negatives at late delay times. Other SkyTEM negatives on the flanks of the anomalies at location 1 (590400E) do not have comparable VTEM negatives, and may be lateral filtering artefacts. If we accept the Eadie and Prikhodko (2013) conclusion that the VTEM raw data is less noisy than SkyTEM in this test, there would be depth of investigation and lateral resolution differences between the two systems. A factor of 4 lower in noise level would correspond to a depth of investigation improvement of at most 40% for horizontal layers, and maybe a 20% increase in depth of exploration for finite conductors. Whether the greater depth of exploration of VTEM, coupled with better lateral resolution and greater confidence in small anomalies is valuable in a cost-benefit analysis is beyond the scope of this review.

Figure 17a shows the effect of 30 m (about 1 second) of lateral averaging on the observed z component double-dipole AEM response of a shallow target, as well as the effect of one example trapezoidal averaging (30 m early to 300 m late) on (b) vertical and (c) horizontal conductors. For significantly deeper conductors, trapezoidal averaging will have less effect on profile shapes than that shown in Figure 17. In any quasi-layered environment, typical of groundwater studies and sediment or regolith mapping, trapezoidal averaging can be justified in terms of the expanding diameter of the induced "smoke ring" of current. However, in mineral exploration where the target is often compact, or steeply dipping, such a windowing scheme distorts and widens anomaly shapes as seen in Figure 16. It may significantly reduce the amplitude of the detected response at later delays, and eliminate the zero directly above a vertically dipping conductor, as the averaging window is wider than the spatial width of the anomaly.

If averaged data is to be inverted, it is easy to filter the model with the same averaging filter as was applied to the data. Without this, fitted conductors would likely be too deep and / or too wide. This is a very good reason to demand details of filtering applied to AEM data, exactly in the same way that all seismic data has its filtering and processing history attached. Adaptive filtering without monitoring leads to unknown filtering and anomaly distortions. A sensible alternative is to request fixed-width (non-adaptive, non-trapezoidal) processing from the contractor, which data are better suited to modelling and anomaly interpretation, and which is an option in data processing software.

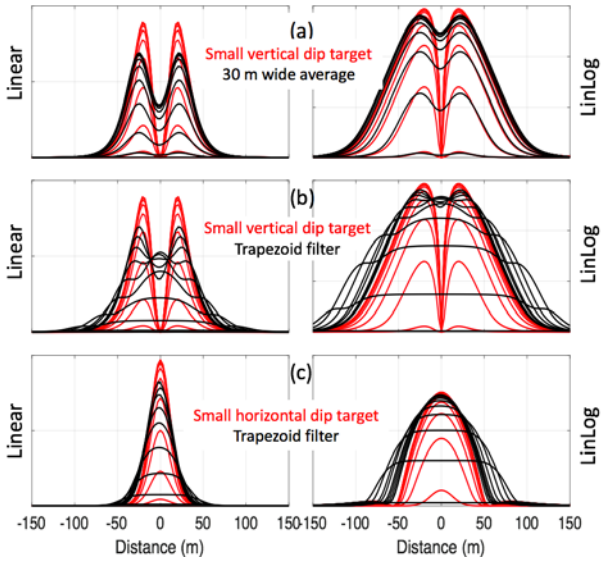

Figure 17: Effect on shape as plotted on linear and linlog scales of 1.5 S small shallow target double-dipole AEM z component response for (a) vertical dip with 30 m averaging, (b) vertical dip with trapezoidal averaging width ranging from 30 m to 150 m, and (c) horizontal dip with trapezoidal averaging range from 30 m to 150 m.

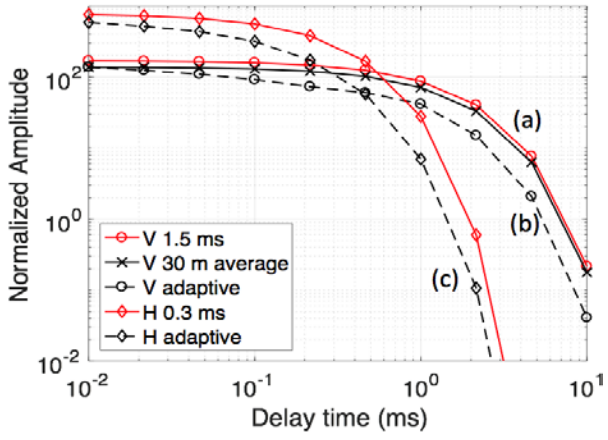

Figure 18: Effect on observed anomaly amplitude decay for the maximum of the responses shown in Figure 17. Symbols (a), (b) and (c) correspond to the Figure 17 profile numbers with V and H referring to the vertical and horizontal target respectively.

One further complication of trapezoidal averaging of a finite targets response is the effect on the observed decay, plotted in Figure 18. Wider, late-time averages cause a greater reduction

in sampled amplitude as seen in (b) and (c), when compared to their respective unfiltered decays in red. Simple averaging (a) of say 30 m results in a small amplitude reduction and slight lateral smoothing without significant decay distortion. Any 2D or 3D modelling or inversion needs to know the precise details of the filter applied at every anomaly, so automatic adaptive filtering without recording the actual filter used at every anomaly is inappropriate for most mineral exploration targets. Decays such as (b) or (c), becoming faster than an exponential decay, could incorrectly be attributed to IP effects in AIP software modelling (Kaminsky and Viezzoli, 2017, Macnae, 2016b).

If targets are extensive and sub-horizontal, adaptive averaging and the advances in laterally and spatially constrained inversion are well documented in the literature (Vignoli et al., 2014). In these cases, adaptive averaging can be valuable methodology that improves the accuracy of the conductivity model outcome.

THE FUTURE

The measurement rather than calculation of vector B fields in AEM is likely to become routine in the next decade with induction magnetometers and possible SQUIDS. Slightly lower base frequencies of 12.5 or 15 Hz may become common, without much loss of resolution or accuracy at early delays if complex PRBS or similar waveforms are used. 6 and even 3 Hz systems are being tested, and may prove to be viable for better AIP and excellent conductor detection in the next decade. Very significant advances in noise reduction through modified waveforms and processing have recently been published (e.g. Velikin and Velikin, 2016) in the Russian literature, and may well improve late delay time signal to noise ratios over the next decade by an order of magnitude, while maintaining good early delay time results. These waveforms and methods would mitigate the effects expected of reduced stacking at lower repetition rates.

While unmanned aerial vehicles (UAV) are becoming ubiquitous, and the concept of a sensor swarm slaved to a piloted aircraft with a large transmitter has great attraction, the high EM noise levels associated with servo electric motors and generators, as well as navigation and communication equipment suggest to me that these will be a development that is very unlikely to happen in the next decade. An exception might be for GPR and VLF mapping systems, where sensors are lightweight and narrowband data useful.

Very limited advance is expected in terms of airborne transmitter output, specifically dipole moment and current stability in the immediate future. This may change if dirigibles become economic to operate. Significant advances however should come through rotation or rotation rate monitoring of sensors, where preliminary results have been very positive. Alternatively, several research groups have been attempting the mechanical isolation of sensors from rotation excitations, using fluid suspension systems. Total field magnetic sensors with limited bandwidth have been used to eliminate airborne rotation noise, but are limited to measuring one magnetic component in the direction of the earth's field and at present limited high-frequency sensitivity. A worthwhile advance proven in theory in the 1990s but only implemented in data acquisition for the ZTEM airborne tilt-angle system is the use of local and remote EM base-stations to help predict and hence remove the effects of unwanted signals.

CONCLUSIONS

The first decade of the 2000s saw helicopter time-domain AEM systems come of age. Since then, advances in suspension systems, electronics and digital processing have lowered noise levels by over an order of magnitude. There have been modest increases in dipole moment, up to about a factor of 2. The breakthroughs that may have just occurred are in acquisition of better low-frequency AEM data. I predict the biggest breakthrough over the next decade will be the development of B field airborne sensors to increase sensitivity to excellent conductors and optimized processing for low-frequency AEM sub 10 Hz in order to remove rotation noise. These developments will improve the search for nickel and massive sulphide deposits. Overall system improvements mean that 1D, 2D and 3D imaging and inversion methodologies will lead to much better geological interpretations.

In summary:

1) Noise: Despite order of magnitude reductions in system noise since the turn of the century, much more can usefully be done in reducing the effects of motion, cultural, system and atmospheric noise. Further coil, SQUID or inductive magnetometer sensor internal noise reductions are not presently needed, as these are the smallest contributor to overall noise. Total field magnetometer noise and limited bandwidth both however could usefully be improved.

2) Signal: Limited increases in dipole moment and Liu waveform factor (Liu, 1998) have improved late-time signals, but the major improvements obtained in ground data with PRBS and composite waveform systems, as well as the slow decay and AIP response characterization of B field sensors are not yet commercial. Wide bandwidth is good for interpretation, but only if signal to noise levels are adequate.

3) SPM effects are now better understood in terms of a very small ferromagnetic particle size distribution, centred around 10 nm. Natural SPM sources have been identified in soil and the seafloor as the result of biogenic bacteria, as well as very thin layers in regolith from burning leaf-litter in bushfires. In volcanic terrains, various tuffs, glasses and chilled margins of intrusions all show SPM.

4) Inductive AIP effects are now commonly seen in data as signal to noise has improved in AEM systems. At the high frequencies of AEM compared to ground galvanic IP, detectable polarizable material may be frozen water in high porosity permafrost conditions, fine grained clays, and fine grained sulphides. Physical property measurements show that the Cole-Cole time constants of most economic sulphides are too long to be energized and detected by AIP, but that AIP may be sensitive to "haloes" around such mineralization.

5) Calibration and QC. 1D test sites such as Lyngby in Denmark are useful for consistency checking, and ensuring that different

AEM systems can be inverted to a common model. 2D or 3D comparisons over small conductors are very useful to characterize the often undisclosed or unknown adaptive lateral averaging in AEM systems. For inversion and modelling of finite targets, adaptive and trapezoidal averaging is not desirable as it distorts both anomaly shapes and decays.

ACKNOWLEDGEMENTS

I thank Osisko Mining for permission to use the SkyTEM and VTEM data used in Figures 5 and 7. Peter Fullagar and Doug Oldenburg are thanked for their detailed and constructive reviews which greatly improved both the perspective and content of this paper. The sponsors of AMIRA projects P1036 and P1036a, Anglo-American, BHPBilliton, Teck-Cominco, Abitibi Geophysics, Outer-Rim Exploration, Monex Geoscope and Thomson Aviation have supported significant research into airborne IP.

REFERENCES

Aarhus University, 2011, Guide for processing and inversion of SkyTEM data in the Aarhus Workbench;; awww.hgg.geo.au.dk/rapporter/guide_skytem_proc_inv.pdf, accessed 1 June 2017.

Annan, A.P. 1986, Development of the PROSPECT I airborne electromagnetic system, in G.J. Palacky, ed., Airborne resistivity mapping: Geological Survey of Canada, Paper 86-22, 63-70.

Asten M., and A. Duncan, 2012, The quantitative advantages of using B-field sensors in time-domain EM measurement for mineral exploration and unexploded ordnance search: Geophysics, 77(4), WB137.

Auken, E., A. Vest Christiansen. J. Westergaard, C. Kirkegaard, N. Foged and A. Viezzoli, 2009, An integrated processing scheme for high-resolution airborne electromagnetic surveys, the SkyTEM system: Exploration Geophysics, 40, 184–192.

Buselli, G., H.S. Hwang, and J.P. Pik, 1998, AEM noise reduction with remote referencing: Exploration Geophysics, 29, 71–76.

Cattach, M.K., J. Stanley, S.J. Lee, and G. Boyd, 1993, Sub-Audio Magnetics (SAM) high resolution technique for simultaneously mapping electrical and magnetic properties: Exploration Geophysics, 24, 387–400.

Chen, T., G. Hodges, and P. Miles, 2015, MULTIPULSE – high resolution and high power in one TDEM system: Exploration Geophysics, 46(1) 49-57.

Chen, C., F. Liu, J. Lin, K. Zhu, and Y Wang, 2016, An Optimized Air-Core Coil Sensor with a Magnetic Flux Compensation Structure Suitable to the Helicopter TEM System; Sensors, 16 (4), 508.

Chikazumi, S. and S.H. Charap, 1978, Physics of Magnetism: Oxford University Press on Demand.

Combrinck, M., 2010, The impact of AEM receiver noise levels on detection, discrimination and resolvability of conductive targets: ASEG Extended Abstracts 2010, 1-4.

Davis, A., and J. Macnae, 2008, Quantifying AEM system characteristics using a ground loop: Geophysics, 73(4), F179-F188.

Davis, A., J. Macnae, and G. Hodges, 2009, Predictions of bird swing from GPS coordinates: Geophysics, 74 (6), F119-F126.

Eadie, T., and A. Prikhodko, 2013, VTEM-SkyTEM^{508} survey comparison over Valen Cu-Ni deposit, Geotech.ca website downloaded 16 May 2017.

Effersø, F., and K. Sørensen, 2013, SkyTEM case study: the Valen survey comparison with VTEM, skytem.com website, downloaded 16 May 2017.

Flores, C., and S. A. Peralta-Ortega, 2009, Induced polarization with in-loop transient electromagnetic soundings: a case study of mineral discrimination at El Arco porphyry copper, Mexico: Journal of Applied Geophysics, 68, 423 – 436.

Foged, N., E. Auken, A. V. Christiansen, and K Sørensen, 2013, Test-site calibration and validation of airborne and ground-based TEM systems: Geophysics, 78(2) E95-106.

Fountain, D., 1998, Airborne electromagnetic systems – 50 years of development: Exploration Geophysics, 29, 1-11.

Fullagar, P., G. Pears, J. Reid, and R. Schaa, 2015, Rapid approximate inversion of airborne TEM: Exploration Geophysics, 46, 112-117.

Gaucher, F., and R. Smith, 2017, The impact of magnetic viscosity on time-domain electromagnetic data from iron oxide minerals embedded in rocks at Opemiska, Québec, Canada; Geophysics, DOI: 10.1190/geo2017-0153.1.

Goold, J., L. Cox, and M. Zhdanov, 2007, Spectral complex conductivity inversion of airborne electromagnetic data: 77th Annual International Meeting, SEG, Expanded Abstracts, 487-491.

Groom, RW., R.Z. Jia, and B. Lo, 2004, Magnetic compensation of magnetic noises related to aircraft's maneuvers in airborne survey: Environ. Eng. Geophys. Soc., 9(1), 101–108.

Hennessy, L., and J. Macnae, 2015, Natural field electro-magnetics using a partially known source: Improvements to signal to noise ratios: ASEG Extended Abstracts 2015, 1-4.

Hine, K., and J. Macnae, 2016, Comparing Induced polarization responses from inductive airborne and galvanic ground systems, Lewis Ponds, NSW: Geophysics, 81(6) B179-188.

Hodges, G., and T. Chen, 2014, IP effect in Airborne TDEM data: Model studies and field examples: 84th Annual International Meeting, SEG, Expanded Abstracts 2014: 828-832.

Hodges, G., and T. Chen, 2015, Geobandwidth: comparing time domain electromagnetic waveforms with a wire loop model: Exploration Geophysics, 46(1) 58-63.

Huang H., and D. Fraser, 2001, Mapping of the resistivity, susceptibility, and permittivity of the earth using a helicopter-borne electromagnetic system: Geophysics, 66 (1), 148-157.

Jaroszewicz, L., A. Kurzych, Z. Krajewski, P. Marć, J. Kowalski, P. Bobra, Z. Zembaty, B. Sakowicz, and R. Jankowski, 2016, Review of the Usefulness of Various Rotational Seismometers with Laboratory Results of Fibre-Optic Ones Tested for Engineering Applications: Sensors (Basel), 16(12), 2161.

Kaminski, V., and A. Viezzoli, 2017, Modeling induced polarization effects in helicopter time-domain electromagnetic data: Field case studies: Geophysics, 82(2), B49-B61.

Kang, S., D. Fournier, and D. Oldenburg, 2017, Inversion of airborne geophysics over the DO-27/18 kimberlites, Part III: Induced Polarization: Interpretation, doi: 10.1190/int-2016-0141.1.

Kolaj, M. and R. Smith, 2013, Using spatial derivatives of electromagnetic data to map lateral conductance variations in thin-sheet models: Applications over mine tailings ponds: Geophysics, 78(5), E225-E235.

Kolaj, M. and R. Smith, 2017, Inductive electromagnetic data interpretation using a 3D distribution of 3D magnetic or electric dipoles: Geophysics, 82(4), E187-E195.

Konieczny, G., A. Smiarowski, and P. Miles, 2016, Breaking through the 25/30 Hz barrier: Lowering the base frequency of the HELITEM airborne EM system: 86th Annual International Meeting, SEG, Expanded Abstracts, 2218-2222.

Kozhevnikov, N.O., and E. Antonov, 2011, The magnetic relaxation of a horizontal layer: Russian Geology and Geophysics 52, 398-404.

Kratzer, T., J. Macnae and P. Mutton, 2012, Detection and correction of SPM effects in airborne EM surveys: Exploration Geophysics, 44, 6-15.

Kratzer, T and J Macnae, 2013, Prediction and removal of rotation noise in airborne EM systems: Exploration Geophysics, 45 (3), 147-153.

Kuzmin, P., and E. Morrison, 2011, Double-suspension receiver coil system and apparatus: US patent 8030933 B2.

Kwan, K., A. Prikhodko, J. Legault, G. Plastow, J. Xie, and K. Fisk, 2015, Airborne inductive induced polarization chargeability mapping of VTEM data: ASEG Extended Abstracts 2015, 1-4.

Lane R., A. Green, C. Golding, M. Owers, P. Pik, C. Plunkett, D. Sattel, and B. Thorn, 2000, An example of 3D conductivity mapping using the TEMPEST airborne electromagnetic system: Exploration Geophysics, 31, 162-172.

Lee, T., 1984, The transient electromagnetic response of a magnetic or superparamagnetic ground: Geophysics, 49, 854–860.

Lee, J., R.J. Turner, M.A. Downey, A. Maddever, D.L. Dart, C.P. Foley, R. Binks, C. Lewis, W. Murray, G. Panjkovic, and M. Asten, 2001, Experience with SQUID magnetometers in airborne TEM surveying: Exploration Geophysics, 32(1) 9 – 13.

Ley-Cooper, Y., and J. Macnae, 2007, Amplitude and phase correction of helicopter EM data: Geophysics, 72(3), F119-F126.

Liu, G. 1998, Effect of transmitter current waveform on airborne TEM response: Exploration Geophysics, 29, 35-41.

Macnae, J., 2007, Developments in broadband airborne electromagnetics in the past decade, in Milkereit, B., ed., Proceedings of Exploration 07, 387-400.

Macnae, J., and S. Baron-Hay, 2010, Reprocessing strategy to obtain quantitative early time data from historic VTEM surveys: ASEG Extended Abstracts 2010.

Macnae, J., 2015, Stripping very low frequency communication signals with minimum shift keying encoding from streamed time-domain electromagnetic data: Geophysics 80(6), E343–E353.

Macnae J. and K. Hine, 2016, Comparing airborne inductive and ground induced polarization: a case history from Western Tasmania: Geophysics, 77(6) E471-480.

Macnae J., 2016a, Definitive superparamagnetic source identification through spatial, temporal and amplitude analysis of airborne electromagnetic data: Geophysical Prospecting online, doi:10.1111/1365-2478.12463

Macnae, J., 2016b, Quantitative estimation of intrinsic induced polarization and superparamagnetic parameters from airborne electromagnetic data: Geophysics ,81 (6), E433-E446.

Macnae, J., 2016c, Fitting superparamagnetic and distributed Cole-Cole parameters to airborne electromagnetic data: A case history from Quebec: Geophysics, 81 (6), B211-B220.

Macnae, J., and L. Hennessy, 2017, Magnetic field sensors for EM geophysics: Presented at Advances in Geophysical Technology Workshop, Exploration 17.

Macnae J., D. Massie, and P. Rogerson, 2017, Towards an Extremely Low Frequency AEM system with AIP capability: BIPTEM: SAGA conference proceedings.

Marchant D., E. Haber, and D.W. Oldenburg, 2014, Three-dimensional modeling of IP effects in time-domain electromagnetic data: Geophysics, 79(6), E303-E314.

Munkholm, M.S., 1997, Motion-induced noise from vibration of a moving TEM detector coil: characterization and suppression: Journal of Applied Geophysics, 37, 21–29.

Néel, L., 1949, Theory of ferromagnetic magnetic drag grained applications with the terracotta: Annals of Geophysics, 2, 99-136.

Nordsiek S., and A. Weller, 2008, A new approach to fitting induced-polarization spectra: Geophysics, 73(6), F235-F245.

Nyboe, N., and K. Sørensen, 2012, Noise reduction in TEM: Presenting a bandwidth- and sensitivity-optimized parallel recording setup and methods for adaptive synchronous detection: Geophysics, 77(3), E203-E212.

Pelton, W.H, S.H. Ward., P.G. Hallof, W.R. Sill and P.H. Nelson, 1978, Mineral discrimination and removal of inductive coupling with multi-frequency IP: Geophysics, 43, 588–609.

Pisane, K., E.C. Despeaux, and M.S. Seehra, 2015, Magnetic relaxation and correlating effective magnetic moment with particle size distribution in maghemite nanoparticles: Journal of Magnetism and Magnetic Materials, 384 148–154.

Sattel, D. and P. Mutton, 2015, Modelling the superparamagnetic response of AEM data: Exploration Geophysics, 46(1) 118-129.

Schamper, C., E. Auken, and K. Sørensen, 2012, A new processing system for very early time mini SkyTEM (SkyTEM101) data: ASEG Extended Abstracts 2012.

Schamper, C., E. Auken, and K. Sørensen, 2014, Coil response inversion for very early time modelling of helicopter-borne time-domain electromagnetic data and mapping of near-surface geological layers: Geophysical Prospecting, 62, 658–674.

Skomski, R., G. Hadjipanayis, and D. Sellmyer, 2007, Effective demagnetizing factors of complicated particle mixtures: IEEE Transactions on Magnetics, 43(6), 2956-2958.

SkyTEM, 2014, http://skytem.com/wp-content/uploads/SkyTEM516-over-Caber-Deposits.pdf, accessed June, 2017.

Slattery, S., and A. Andriashek, 2012, Overview of airborne electromagnetic and magnetic geophysical data collection using the GEOTEM Survey North of Calgary, Alberta; Energy resources conservation board: Open File Report 2012-09.

Smiarowski, A., and J. Macnae, J., 2013, Detection of a perfect conductor with an airborne electromagnetic system: The Gemini Field Test": Geophysics, 78(5), E249 - E259.

Smiarowski, A., and P. Miles, 2015, Apparatus and method for compensating for receiver motion in airborne electromagnetic systems: PCT/IB2015/002482.

Smith, R. and J. Klein, 1996, A special circumstance of airborne induced-polarization measurements, Geophysics, 66(1), 66-73.

Sørensen, K., and E. Auken, 2004, SkyTEM – a new high-resolution helicopter transient electromagnetic system: Exploration Geophysics, 35(3), 194-202.

Stillman, D., R. Grimm, and S. Dec, 2010, Low-Frequency Electrical Properties of Ice-Silicate Mixtures: J. Phys. Chem. B, 114, 6065–6073.

Sunderland, A., R. Lockwood, L. Ju, D. Blair, 2017, Low-frequency rotational isolator for airborne exploration: Geophysics, 82(2), E27-E30.

Tarasov, L., 1938, Demagnetization Coefficient of Oblate Spheroids: Physical Review, 53, 105.

Tarasov, A. and K. Titov, 2013, On the use of the Cole-Cole equations in spectral induced polarization: Geophys. J. Int., 195, 352-356, with comment by Macnae: Geophys. J. Int., 202 (1), 529-532.

Valleau, N.C., 2000, HEM data processing: a practical overview: Exploration Geophysics 31(4), 584–594.

Babu, V.R., I. Patra, S. Tripathi, S. Muthyala, and A.K. Chaturvedi, 2017, Restricted access Inductive induced polarization effect in heliborne time-domain electromagnetic data for uranium exploration, northern part of Cuddapah Basin, India: Geophysics, 82(3), 1-44.

Velikin A. and A. Velikin, 2016, The results of field testing of the correlation method of pulse electromagnetic prospecting systems STEM: Geology & methodics of prospect and exploration of deposits, (3), 31-38 (In Russian).

Vignoli G., G. Fiandaca, A.V. Christiansen, C. Kirkegaard, and E. Auken, 2015, Sharp spatially constrained inversion with applications to transient electromagnetic data: Geophysical Prospecting, 63, 243–255.

Vrbancich, J., J. Macnae, D. Sattel, and P. Wolfgram, 2005, A case study of AEM bathymetry in Geographe Bay and over Cape Naturaliste, Western Australia, Part 2: 25 and 12.5 Hz GEOTEM: Exploration Geophysics, 36, 381–392.

Vrbancich, J., and R. Smith, 2005, Limitations of two approximate methods for determining the AEM bird position in a conductive environment: Exploration Geophysics, 36, 365 – 373.

Wang, L., B. Li, J. Lin, Q. Wang, Y. Cheng, and K Zhu, 2015, Noise removal based on filtered principal component reconstruction: Chinese Journal of Geophysics, 58, 589–598.

Weigand, M. and A. Kemna, 2016, Relationship between Cole–Cole model parameters and spectral decomposition parameters derived from SIP data: Geophysical Journal International, 205(3), 1414-1419.

Wong, J., 1979. An electrochemical model of the induced polarization phenomenon in disseminated sulfide ores: Geophysics, 44, 1245-1265.

Yang, D., and D.W. Oldenburg, 2016, 3D inversion of total magnetic intensity data for time-domain EM at the Lalor massive sulphide deposit: Exploration Geophysics, 48(2), 110-123.

Yin, C., and G. Hodges, 2009, Wire-loop surface conductor for airborne EM system testing: Geophysics, 74(1), F1-F8.

Ziolkowski, A., D. Wright and J. Mattson, 2011, Comparison of pseudo-random binary sequence and square-wave transient controlled-source electromagnetic data over the Peon gas discovery, Norway: Geophysical Prospecting, 59, 1114-1131.